Modelling, Simulation and Control of two Hybrids between a Quadrotor and a Fixed Wing Aircraft

Bruno Miguel Gomes de Oliveira
bruno.miguel.oliveira@tecnico.ulisboa.pt

Instituto Superior Técnico, Universidade de Lisboa, Lisboa, Portugal

June 2017

Abstract

The past decade saw the boom of Vertical Take-Off and Landing (VTOL) vehicles, such as quadrotors, hexarotors, and similar. But in more recent years there has been growing interest in vehicles that can take off vertically, and capable of flying like an airplane, to overcome some of the limitations of multirotors.

The present work provides a preliminary analysis of these types of vehicles, to assess their advantages and disadvantages.

First, two different approaches to these types of vehicles are selected, to provide a wider view of what can be accomplished. And for those vehicles, an extensive dynamic and kinematic model is obtained. Due to the specific working conditions of these vehicles, a more advanced model for the propellers than the traditionally used for quadrotors is obtained.

With the complete model for the vehicles, an analysis on the vehicles dynamics and range, for varying airspeed is performed.

Finally, a control strategy capable of dealing with the peculiarities of these vehicles is proposed and tested.

1 Introduction

Quadrotors and unmanned airplanes are both widely used nowadays. Quadrotors for tasks such as recording events from the air or high voltage poles inspection. And unmanned airplanes for long range surveillance, or transport. But still, there are scenarios where none of those vehicles fit the needs.

To fill that space, hybrid vehicles are looked at, to overcome some of the limitations of both types of vehicles. Many approaches have been proposed; William J. Fredericks *et al.* [1], at the NASA Langley Research Center, performed an analysis of 4 different vehicles, to assess their feasibility and expected performance.

The MAVion [2] is in development at the Institut Supérieur de l'Aéronautique et de l'Espace since 2009, intended to be a vehicle capable of operating in complex urban environments, both outdoor and indoor.

In [3] another type of vehicle is proposed, one where only the propellers rotate to transition from Axial flight to Forward flight. A model for the propellers is derived based on the Blade Element Theory. For the wings linear and quadratic approximations for the lift and drag coefficients were considered, as they will not be subject to large angles of attack. To control the vehicle, 2 controllers are obtained, switching between them depending on the propellers tilt.

One of the main objectives of the present work is to obtain a model that describes comprehensibly the dynamics of these types of vehicles. It is also

intented to carry out a preliminary analysis of the vehicles range with different propellers, for varying airspeed. And last, implement a control strategy capable of controlling these vehicles throughout their varying working conditions and attitudes.

In section 2 the vehicles and respective models are presented; in section 3 the propeller modeling; in section 4 an analysis on the vehicles range and attitude for varying air speed; in section 5 control strategy obtained is presented; and in section 6 the final conclusions of this work are presented.

2 Vehicle models

The first of the vehicles selected, which will be addressed as Hybrid Quadrotor (fig. 1 left), can be considered more unconventional. Although it has some similarities with an usual quadrotor when it comes to the propulsion system, the structure and operating mode are very different and unique.

The second one, called Hybrid Plane (fig. 1 right), could be considered as a more traditional approach. It can be characterised mainly as a traditional airplane, but with the addition of 4 propellers responsible for the vertical take off and landing, like a quadrotor.

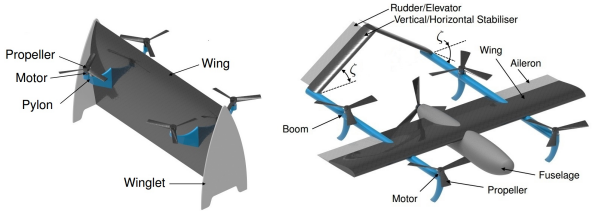

Figure 1: Hybrid Quadrotor, Hybrid Plane

For each vehicle two flight modes are identified: Axial flight, for taking off and landing, and low speed movement; and Forward flight, for higher airspeed flight.

In Axial flight (fig. 2), the propellers of the Hybrid Quadrotor provide all the lift to keep it airborne and to move it, by providing differential thrust. In Forward flight, the wing provides most of the lift, with the propellers responsible for controlling its movement.

In the transition between Axial flight and Forward flight, the vehicle starts moving forward, by leaning in that direction. As it gains speed the wing generates increasingly more lift and the vehicle can be rotated further, until is reaches the Forward flight attitude.

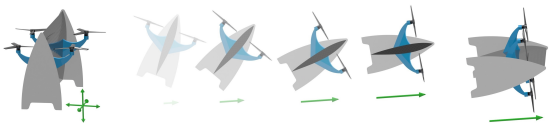

Figure 2: Axial flight, Transition, Forward flight

The Hybrid plane (fig. 3), in Axial flight, behaves similarly, with the 4 vertical propellers to generate lift and control the vehicle. The propeller on the back is turned off. In Forward flight the vehicle is propelled forward with the 5th propeller, with the wing generating lift, and manoeuvred with the control surfaces. The 4 vertical propellers are turned off.

For the transition from Axial flight to Forward flight the back motor is turned on, moving the vehicle forward. As it gains speed and the wing generates lift, the 4 propellers reduce their speed, until the wing generates enough lift and they can be completely turned off.

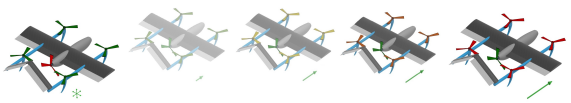

Figure 3: Axial flight, Transition, Forward flight

2.1 Reference Frames: The base reference frame R_0 is defined as NED (North, East, Down). Three reference frames will be defined for each vehicle, identified as Body frame (R_b), Wing frame (R_w) and Aerodynamic Forces frame (R_f), illustrated in figures 4 and 5.

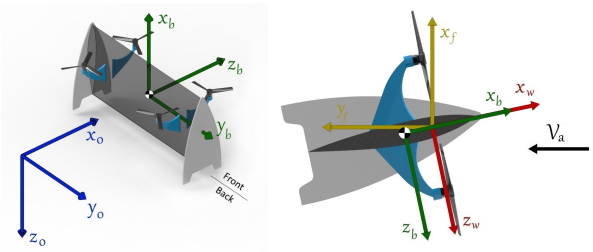

Figure 4: Hybrid Quadrotor reference frames

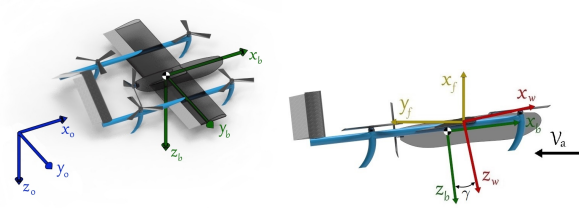

Figure 5: Hybrid Plane reference frames

2.2 Vehicle dynamic and kinematics: The vehicle is subject to various forces, in the present work the main ones are addressed. These are divided into 3 parts: Gravity ($\boldsymbol{F_g}$), Propulsion system ($\boldsymbol{F_p}$, $\boldsymbol{M_p}$), Aerodynamics ($\boldsymbol{F_a}$, $\boldsymbol{M_a}$). The aerodynamic forces and moments are split in two terms, the wing ($\boldsymbol{F_{w_b}}$, $\boldsymbol{M_{w_b}}$) and the body ($\boldsymbol{F_{e_b}}$, $\boldsymbol{M_{e_b}}$). The vehicle dynamics, following a Newton-Euler approach [4], and assuming constant mass and inertia, may be expressed by the following equations:

$$\begin{aligned} m\dot{\boldsymbol{V}}_b &= -\boldsymbol{\omega}_b \times m\boldsymbol{V}_b + \boldsymbol{F_{g_b}} + \boldsymbol{F_{p_b}} + \boldsymbol{F_{a_b}} \\ \boldsymbol{J_v}\dot{\boldsymbol{\omega}}_b &= -\boldsymbol{\omega}_b \times \boldsymbol{J_v}\boldsymbol{\omega}_b + \boldsymbol{M_{p_b}} + \boldsymbol{M_{a_b}} \end{aligned} \tag{1}$$

where $\boldsymbol{V_b}$ is the vehicle linear speed, $\boldsymbol{\omega_b}$ the angular speed, $\boldsymbol{J_v}$ the vehicle inertia matrix, and $\boldsymbol{F_{g_b}}$ the force vector resulting from the gravity force.

As for the kinematic equations for our vehicle, they are given by :

$$\begin{aligned} \dot{\boldsymbol{p}} &= \boldsymbol{R_b^0 V_b} \\ \dot{\boldsymbol{\eta}} &= -\frac{1}{2}\begin{bmatrix} 0 & \omega_{b,x} & \omega_{b,y} & \omega_{b,z} \\ -\omega_{b,x} & 0 & -\omega_{b,z} & \omega_{b,y} \\ -\omega_{b,y} & \omega_{b,z} & 0 & -\omega_{b,x} \\ -\omega_{b,z} & -\omega_{b,y} & \omega_{b,x} & 0 \end{bmatrix}\boldsymbol{\eta} \end{aligned} \tag{2}$$

With $\boldsymbol{p}$ the position vector, and $\boldsymbol{\eta}$ the vehicle orientation relative to the base reference frame, expressed in unit quaternions.

2.3 Gravity: The gravity force in the body frame is given by $\boldsymbol{F_{g_b}} = \boldsymbol{R_0^b}\, m\, \boldsymbol{g}$, where m is the vehicle mass, and $\boldsymbol{g}$ is the local earth gravity acceleration expressed in the base reference frame.

2.4 Propellers: The formulation and analysis of the model obtained is presented in chapter 3, but a brief summary will be presented here.

Each propeller i rotates at angular speed Ω_i producing thrust T_i and torque Q_i. But given the presence of air flow in the lateral direction of the propeller, there will also be transverse moments M_{i_y} and M_{i_z}.

$$\begin{aligned} T_i &= \rho\pi R_p^2(\Omega_i R_p)^2 C_T \\ Q_i &= \rho\pi R_p^3(\Omega_i R_p)^2 C_P \\ \begin{bmatrix} M_{i_y} \\ M_{i_z} \end{bmatrix} &= \rho\pi R_p^3(\Omega_i R_p)^2 \begin{bmatrix} cos(\beta) & -sin(\beta) \\ sin(\beta) & cos(\beta) \end{bmatrix} \begin{bmatrix} C_{M_y} \\ C_{M_z} \end{bmatrix} \end{aligned} \tag{3}$$

where C_T is the thrust coefficient, C_P the power coefficient, C_{M_x} and C_{M_y} transverse moment coefficients, and β is the angle between the incident lateral air flow and the axis y_b, obtained as $\beta = atan2\big(V_{a_{b,z}}, V_{a_{b,y}}\big)$. The thrust, power and moment coefficients are given by:

$$\begin{aligned} C_T = \frac{N_b c_p}{2\pi R_p}\Bigg(& 2C_{L_\alpha}\sqrt{C_{L_\Delta}}\Bigg[\theta_0\Big(\frac{1}{3}+\mu_{yz}^2\frac{1-r_i}{2}\Big) \\ & + \theta_{tw}\Big(\frac{1}{4}+\mu_{yz}^2\frac{1-r_i^2}{4}\Big) - \lambda\frac{1-r_i^2}{2}\Bigg] \\ & - C_{L_\alpha}^2\Bigg[\theta_0^2\Big(\frac{1}{3}+\mu_{yz}^2\frac{1-r_i}{2}\Big) + \theta_{tw}^2\Big(\frac{1}{5}+\mu_{yz}^2\frac{1}{6}\Big) \\ & + \theta_0\theta_{tw}\Big(\frac{1}{2}+\mu_{yz}^2\frac{1-r_i^2}{2}\Big) + \lambda^2(1-r_i) \\ & - \lambda\theta_0(1-r_i^2) - \frac{2}{3}\lambda\theta_{tw}\Bigg] \\ & + (C_{L_M}-C_{L_\Delta})\Big(\frac{1}{3}+\mu_{yz}^2\frac{1-r_i}{2}\Big)\Bigg) \\ C_P = \frac{N_b c_p}{2\pi R_p}\Bigg(& (C_{L_M}-C_{L_\Delta})\frac{\lambda}{3} - C_{L_\alpha}^2\lambda\Bigg[\theta_0^2\frac{1}{3}+\theta_{tw}^2\frac{1}{5} \\ & + \theta_0\theta_{tw}\frac{1}{2} - \lambda\theta_0 - 2\lambda\theta_{tw}\frac{1}{3} + \lambda^2\Big(\sqrt{1-\mu_{yz}^2} \end{aligned}$$

$$
\begin{aligned}
&- \sqrt{r_i^2}\Big)\Big] + C_{L_\alpha}\sqrt{C_{L_\Delta}}\lambda\Big[2\theta_0\frac{1}{3} + \theta_{tw}\frac{1-r_i^2}{2} \\
&- \lambda(1-r_i^2)\Big] + C_{D_\alpha}\Big[\theta_0^2\Big(\frac{1}{4} + \mu^2\frac{1-r_i^2}{4}\Big) \\
&+ \theta_{tw}^2\Big(\frac{1}{6} + \mu^2\frac{1}{8}\Big) + \lambda^2\frac{1-r_i^2}{2} + \theta_0\theta_{tw}\Big(\frac{2}{5} + \mu^2\frac{1}{3}\Big) \\
&- 2\lambda\Big(\theta_0\frac{1}{3} + \theta_{tw}\frac{1}{4}\Big)\Big] + C_{D_0}\Big[\frac{1}{4} + \mu_{yz}\frac{1-r_i^2}{4}\Big]\Big)
\end{aligned}
$$

$$
\begin{aligned}
C_{M_y} = \frac{N_b c_p}{2\pi R_p}\Bigg(&C_{L_\alpha}^2\Big[\lambda\theta_0\mu_{yz}\frac{1-r_i^2}{2} - \theta_0^2\mu_{yz}\frac{1}{3} \\
&+ \lambda\theta_{tw}\mu_{yz}\frac{1}{3} - \theta_0\theta_{tw}\mu_{yz}\frac{1}{4} - \theta_{tw}^2\mu_{yz}\frac{1}{5}\Big] \\
&- C_{L_\alpha}\sqrt{C_{L_\Delta}}\Big[\lambda\mu_{yz}\frac{1-r_i^2}{2} - 2\theta_0\mu_{yz}\frac{1}{3} \\
&+ \theta_{tw}\mu_{yz}\frac{1}{4} + (C_{L_M} - C_{L_\Delta})\mu_{yz}\frac{1}{3}\Big)
\end{aligned}
$$

$$
\begin{aligned}
C_{M_z} = \frac{N_b c_p}{2\pi R_p}\Bigg(&C_{L_\alpha}\sqrt{C_{L_\Delta}}\lambda_0 k_x\frac{1}{4} + C_{L_\alpha}^2\Big[\lambda_0^2 k_x\frac{1}{3} \\
&- \lambda_0\theta_0 k_x\frac{1}{4} - \lambda_0\theta_{tw}k_x\frac{1}{5} + \lambda_0 k_x\mu_x\frac{1}{3}\Big]\Bigg)
\end{aligned}
\tag{4}
$$

As illustrated in figure 6, the blade has external radius R_p, inner radius R_i and chord c_p. With r_i the dimensionless inner radius, given as $\frac{R_i}{R_p}$. The blade is assumed to have a constant twisting rate, θ_{tw}, obtained as $\theta_{tw} = \frac{\theta_{R_p} - \theta_{R_i}}{R_p - R_i}$, and θ_0 would be the angle of the blade at the axis of the propeller, if R_i was equal to 0, and can be calculated as $\theta_0 = \theta_{R_i} - \theta_{tw}R_i$.

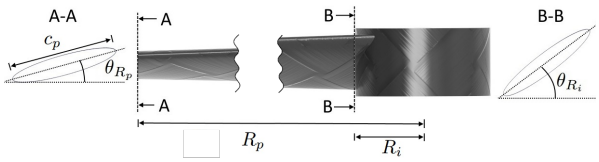

Figure 6: Propeller Blade twisting

The lift coefficient is approximated quadratically, in the form $C_L(\alpha) = C_{L_M} - (C_{L_\alpha}\alpha(R,\psi) - \sqrt{C_{L_\Delta}})^2$. C_{L_M} corresponds to the maximum value, $C_{L_M} - C_{L_\Delta}$ is the function value at α=0, and $2C_{L_\alpha}\sqrt{C_{L_\Delta}}$ is the slope at α=0. The drag coefficient is also approximated quadratically, as $C_D(\alpha) = C_{D_0} + C_{D_\alpha}\alpha^2(R,\psi)$, characterised with drag coefficient form C_{D_α}, and static drag coefficient C_{D_0}. These are illustrated in figure 7.

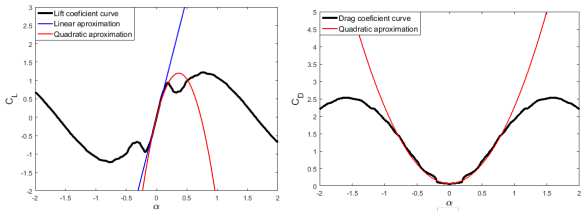

Figure 7: Lift and Drag coefficients approximations

Relative to the air flow at the blades, μ_x is the dimensionless coefficient of the external axial flow, given as $\mu_x = \frac{V_{a_{b,x}}}{\Omega R_p}$, and μ_y is the dimensionless coefficient of the external lateral flow, given as $\mu_y = \frac{\sqrt{V_{a_{b,y}}^2 + V_{a_{b,z}}^2}}{\Omega R_p}$. The inflow [5] can be obtained as $\lambda_0 = \frac{C_T}{2\sqrt{\mu_y^2 + \lambda^2}}$, and $\lambda = \mu_x + \lambda_0$. The variable k_x characterises the unbalance in the inflow, and is given as $k_x = tan(\frac{X}{2})$, with $X = tan^{-1}(\frac{\mu_y}{\mu_x + \lambda_0})$

The propellers are identified in figure 8.

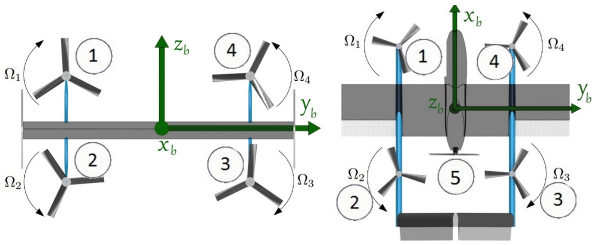

Figure 8: Propeller identification

The resulting propulsion forces and moments for the Hybrid Quadrotor are given by :

$$
\boldsymbol{F_{p_b}} = \begin{bmatrix} \sum_{i=1}^{4} T_i \\ 0 \\ 0 \end{bmatrix}, \boldsymbol{M_{p_b}} = \begin{bmatrix} -\sum_{i=1}^{4} Q_i(-1)^i \\ \sum_{i=1}^{4} T_i z_{i_b} - \sum_{i=1}^{4} M_{i_y}(-1)^i \\ -\sum_{i=1}^{4} T_i y_{i_b} - \sum_{i=1}^{4} M_{i_z} \end{bmatrix}
\tag{5}
$$

with z_{i_b} and y_{i_b} the propeller coordinates in the body reference frame.

And for the Hybrid Plane:

$$\boldsymbol{F_{p_b}} = \begin{bmatrix} T_5 \\ 0 \\ -\sum_{i=1}^{4} T_i \end{bmatrix}$$

$$\boldsymbol{M_{p_b}} = \begin{bmatrix} -\sum_{i=1}^{4} T_i y_{i_b} - Q_5 - \sum_{i=1}^{4} M_{i_x} \\ \sum_{i=1}^{4} T_i x_{i_b} + z_{5_b} T_5 - \sum_{i=1}^{4} M_{i_y}(-1)^i + M_{5_y} \\ \sum_{i=1}^{4} +y_{5_b} T_5 - M_{5_z} + Q_i(-1)^i \end{bmatrix} \tag{6}$$

2.5 Motor: This type of vehicles usually uses brushless DC motors, for their high efficiency and specific power. They can be modeled as a simple DC motor, as follows [6]:

$$\begin{aligned} \frac{\mathrm{d}I_i}{\mathrm{d}t} &= \frac{V_{m_i} - R_m I_i - K_e \Omega_i}{L_m} \\ \frac{\mathrm{d}\Omega_i}{\mathrm{d}t} &= \frac{K_t I_i - Q_i - B_m \Omega_i}{J_m} \end{aligned} \tag{7}$$

where I_i is the current for each motor and V_{m_i} the control voltage. With the properties of the motor-propeller set as follows : circuit resistance R_m, circuit inductance L_m, counter-electromotive force constant K_e, rotor inertia J_m , torque constant K_t and friction constant B_m.

The servo motors considered to actuate the control surfaces in the Hybrid Plane will be considered as nearly instantaneous first order system, with a high value of K_δ, and simply modeled as:

$$\frac{\mathrm{d}\delta_i}{\mathrm{d}t} = (\delta_i^c - \delta_i) K_\delta \tag{8}$$

where δ_i^c corresponds to the command input for each surface, and δ_i the surface deflection angle.

2.6 Wings: The wing of the Hybrid Quadrotor is divided in 2 sections (fig. 9), and in the Hybrid Plane divided in 6 sections (fig. 10)).

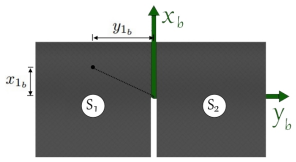

Figure 9: Hybrid Quadrotor Wing sections

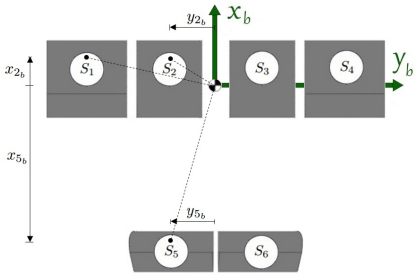

Figure 10: Hybrid Plane Wing sections

The wing aerodynamic forces will be given as:

$$\begin{aligned} L_i &= \frac{1}{2}\rho V_{a,i}^2 A_i C_L(\alpha_i) \\ D_i &= \frac{1}{2}\rho V_{a,i}^2 A_i C_D(\alpha_i) \\ M_i &= \frac{1}{2}\rho V_{a,i}^2 A_i C_M(\alpha_i) \end{aligned} \tag{9}$$

with the coefficients C_L, C_D and C_M represented from $= -180°$ to $180°$ [7]. The effective airspeed on each surface S_i, in the body frame, V_{ef,i_b} is given as :

$$\boldsymbol{V_{ef,i_b}} = \boldsymbol{V_{a_b}} + \begin{bmatrix} 0 & z_{i_b} & -y_{i_b} \\ -z_{i_b} & 0 & x_{i_b} \\ y_{i_b} & -x_{i_b} & 0 \end{bmatrix} \boldsymbol{\omega_b} \tag{10}$$

The effective speed, in the wing frame of each section, and respective angle of attack:

$$\boldsymbol{V_{ef,i_w}} = \boldsymbol{R_{b_i}^w}\ \boldsymbol{V_{ef,i_b}}$$

$$\boldsymbol{R_{b_i}^w} = \begin{bmatrix} cos(i_w) & 0 & -sin(i_w) \\ 0 & 1 & 0 \\ sin(i_w) & 0 & cos(i_w) \end{bmatrix}$$

$$\alpha_i = \Delta\alpha_i + atan2\Big(\big(V_{ef,i_{w,z}} cos(\zeta_i) + V_{ef,i_{w,y}} sin(\zeta_i)\big), V_{ef,i_{w,x}}\Big)$$

$$V_{a,i} = \sqrt{\big(V_{ef,i_{w,z}} cos(\zeta_i) + V_{ef,i_{w,y}} sin(\zeta_i)\big)^2 + {V_{ef,i_{w,x}}}^2} \tag{11}$$

where i_w is the surface incidence angle, and ζ_i the lateral inclination angle.

For the controls surfaces, the approach presented in [8] is adopted, considering the change in angle of attack function of the change in the airfoil chamber.

The resulting forces for each surface, in the body reference frame:

$$\boldsymbol{R}^{\boldsymbol{b}}_{\boldsymbol{f},\boldsymbol{S_i}} = \begin{bmatrix} 1 & 0 & 0 \\ 0 & c(\zeta_i) & -s(\zeta_i) \\ 0 & s(\zeta_i) & c(\zeta_i) \end{bmatrix} \begin{bmatrix} -s(i_w-\alpha_i) & -c(i_w-\alpha_i) & 0 \\ 0 & 0 & 1 \\ -c(i_w-\alpha_i) & s(i_w-\alpha_i) & 0 \end{bmatrix}$$

$$\boldsymbol{F_{i_b}} = \boldsymbol{R}^{\boldsymbol{b}}_{\boldsymbol{f},\boldsymbol{S_i}} \begin{bmatrix} L_i \\ D_i \\ 0 \end{bmatrix} \quad , \quad \boldsymbol{M_{i_b}} = \begin{bmatrix} 0 \\ -M_i \\ 0 \end{bmatrix} \tag{12}$$

And the combined result is:

$$\boldsymbol{F_{w_b}} = \sum_i \boldsymbol{F_{i_b}}$$

$$\boldsymbol{M_{w_b}} = \sum_i \boldsymbol{M_{i_b}} + \sum_i \begin{bmatrix} 0 & -z_{i_b} & y_{i_b} \\ z_{i_b} & 0 & -x_{i_b} \\ -y_{i_b} & x_{i_b} & 0 \end{bmatrix} \boldsymbol{F_{i_b}} \tag{13}$$

3 Propeller Modeling

The model for the propeller was derived using the Blade Element Theory (BET) and Momentum Theory, following the usual analysis for helicopters [5]. The blade is divided into infinitesimal sections along the radius and analysed similarly to the wing (fig 11).

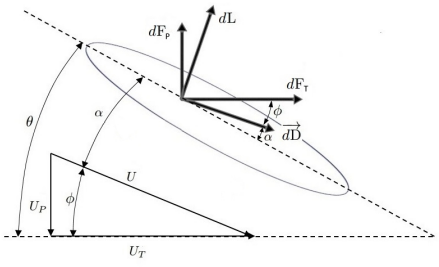

Figure 11: Propeller Blade aerodynamics, [5]

Considering the external airflow, the incidence angle, and the propeller inflow (fig 12).

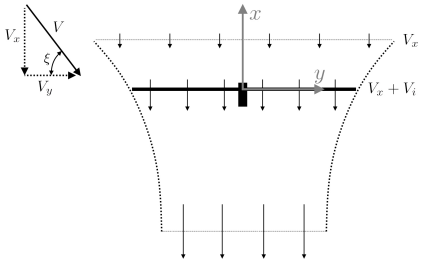

Figure 12: Propeller Inflow

7 models were compared, with various degrees of approximation. The final model selected corresponds to Model 6, with the following simplifications:

$U(R,\psi) = \sqrt{U_T^2(R,\psi) + U_P^2(R,\psi)} \approx U_T(R,\psi)$		
$U_T(R,\psi) = \Omega R + V_{yz} sin(\psi)$		
$\phi(R,\psi) = tan^{-1}\left(\frac{U_P}{U_T}\right) \approx \frac{\lambda}{r + \mu_{yz} sin(\psi)}$		
$sin(\phi(R,\psi)) \approx \phi(R,\psi)$	$dD\ \phi(R,\psi) \approx 0$	
$cos(\phi(R,\psi)) \approx 1$	$k_x = tan\left(\frac{X}{2}\right)$	
$X = tan^{-1}\left(\frac{\mu_y}{\mu_x + \lambda_0}\right)$	$\lambda = \mu_x + \lambda_i$	
$\lambda_i(R,\psi) = \lambda_0(1 + k_x r cos(\psi))$		
$\mu_x = \frac{V_x}{\Omega R_p}$	$\mu_y = \frac{V_y}{\Omega R_p}$	$\lambda_i(R,\psi) = \frac{V_i(R,\psi)}{\Omega R_p}$

The different approximations affect mainly in two areas. First, in the case of high pitch propellers, with the approximation used for the lift coefficient. Second, the unbalance in the forces across the propeller disk, leading to the generation of moments.

3.1 Analisys The linear approximation for the lift coefficient, used in models 1 to 5, leads to an unrealistic continuous increase of thrust coefficient, which would provide a better efficiency at low advance ratios than low pitch propellers.

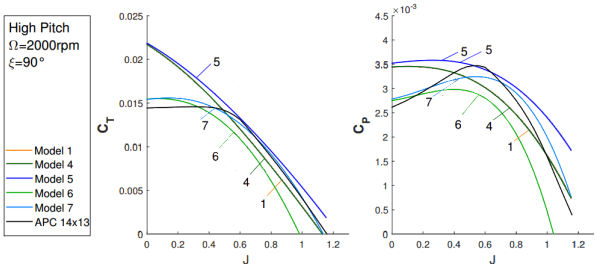

Figure 13: Dimensionless coefficients, $\Omega = 2000$rpm, $\xi = 90°$, high pitch, models 4 to 7

The unbalances in the forces due to the lateral external airflow and the inflow generate C_{M_y} and C_{M_z}.

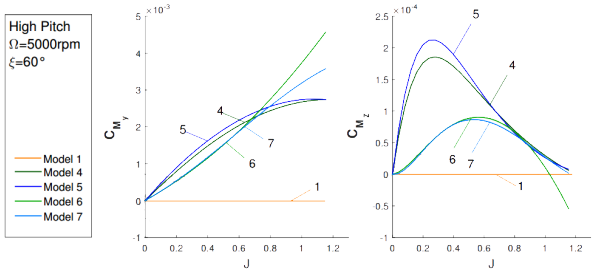

Figure 14: Dimensionless coefficients, $\Omega = 2000$rpm, $\xi = 90°$, high pitch, models 4 to 7

Those unbalances can be seen in figure 15. It shows the distribution of thrust coefficient across the propeller disk. In both models 4 and 6 there is a displacement of the maximum thrust to the advancing side.

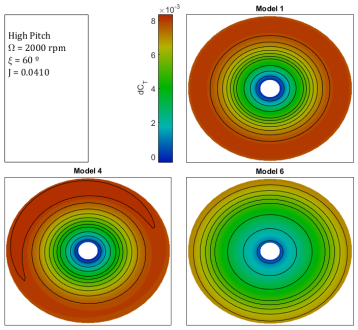

Figure 15: Disc distribution analysis of dC_T and α, depending on the models

The effects of the lift coefficient approximation are also visible. In model 6, the thrust generated across the propeller is smaller, and more towards the outer section.

In figure 16 the same analysis with respect to the angle of attack is presented. The angle of attack is higher in models 6 as a result of the lower thrust, and consequent lower inflow.

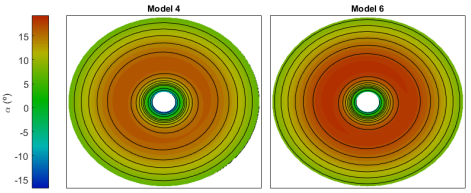

Figure 16: Disc distribution analysis of dC_T and α, depending on the models

At high values of J the effects in the thrust unbalance are greater, as shown in figure 17.

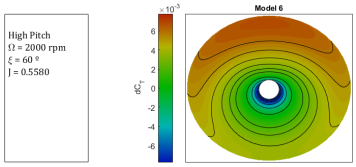

Figure 17: Disc distribution analysis of dC_T and α, depending on the models

4 Trim Flights vs Airspeed

The low pitch propellers provide the highest efficiency for Axial flight, and both medium and high pitch propellers give the highest range at Forward flight. For the Hybrid Quadrotor, the propellers selected are the 14×10. They provide range close to the best high pitch propellers, with only a reduction of 25% in flight time at low speeds.

In the Hybrid Quadrotor, a peak appears (fig. 17), when the vehicle, and consequently the wing, reach an angle around $12°$ (fig. 19). At that angle the wing drag is significantly reduced, leading to a large spike in range.

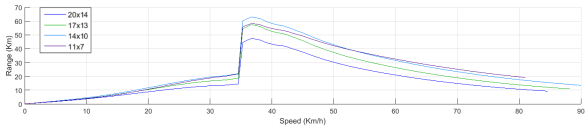

Figure 18: Hybrid Quadrotor trim vs airspeed, with medium pitch propellers

For the Hybrid Plane, the propellers selected are the 17×8 for propellers 1 to 4, as it provides the highest efficiency for Axial flight and for the transition. For the 5th propeller, a 14×10 propellers is chosen.

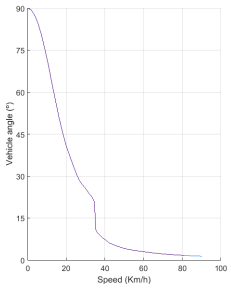

Figure 19: Hybrid Quadrotor trim vs airspeed, with medium pitch propellers

5 Control Design

The vehicles are controlled using a Linear-Quadratic Regulators (LQR), and by separating the flight in 3 areas: Axial flight, Transition, and Forward flight. To that end, the dynamic linear modes of the vehicles in those scenarios is obtained.

For the Hybrid Quadrotor, 2 matrices from the Axial flight system matrix are obtained, one for the start and another to stop. The first one enables an easy transition from Axial flight to Forward flight, and the second guarantees a more stable stop. From transition and Forward flight system matrices we obtain one control matrix for each. In the case of the hybrid plane one control matrix from each of the 4 system matrices is obtained.

The control strategy proposed in this work is composed of 3 levels (fig. 20).

In the inner loop we have LQR matrices, weighted by coefficients depending on the air speed and distance to target. In both vehicles, a distance of 20 meters was set as the limit from target to change the type of flight. If the vehicle is located further than that distance from the target it will transition to aerodynamic fight, and as it reaches that distance it will start to transition to Axial flight. If the vehicle starts already at less than 20m it will never transition to Forward flight.

In the outer loop, the controller takes the desired position and calculates the desired speed V_T and orientation. The maximum desired speed is considered $13m/s$, to keep the vehicle working near the maximum efficiency. The desired orientation is limited to a maximum offset of $\frac{pi}{16}$ $radians$ from the current orientation. Due to the unitary nature of quaternions, with a big difference in one of the entries, the others will also be affected in value, leading to a false actuation.

In the intermediate controller level, the state is subtracted to the references obtaining the feedback error $\boldsymbol{e_i} = \boldsymbol{x_{ref_i}} - \boldsymbol{x}$ for each of the four LQRs identified as $i = [1.1\ 1.2\ 2\ 3]$, where $\boldsymbol{x_{ref_i}}$ is the state space reference vector for each controller.

5.1 Results Hybrid Quadrotor: Performing a complete flight, from Axial flight to Forward flight and from Forward flight back to Axial flight some small instabilities appear, that were expected due to the use of discrete curves with irregularities for the wings coefficients. The controllers are also part responsible for the small oscillations, as they need to allow the vehicle to move away from the equilibrium position to transition to the next controller.

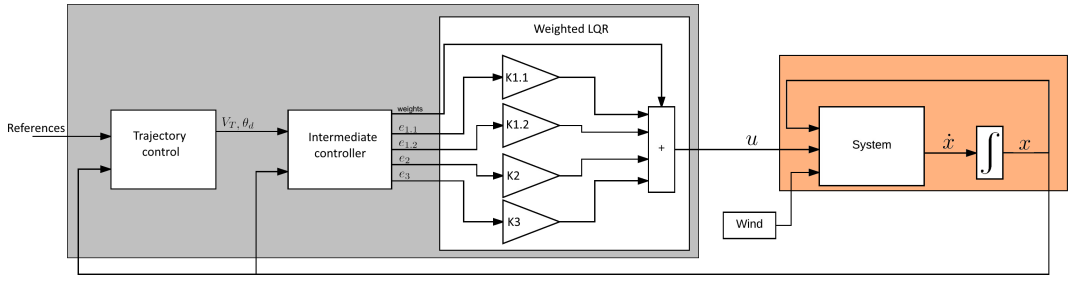

Figure 20: Control strategy plant

The vehicle starts from position $[NED] = [0\ 0\ 0]$, with z_b oriented with x_0 (fig. 23). The target point is $[10\ \ -150\ 0]$, with no fixed orientation.

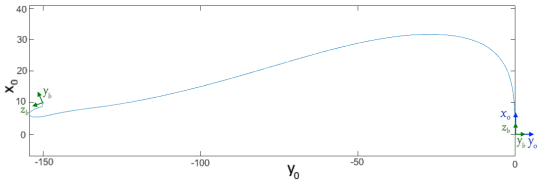

Figure 21: Hybrid Quadrotor horizontal flight path

As the vehicle transitions from Axial flight to Forward flight it quickly gains forward speed (fig. 24) and transitions to Forward flight attitude. This fast transition is obtained by maxing out the motors. The speed V_x is keep near the target of $13\ m/s$, but during the turn, due to the rotation, the controller has more difficulty in attaining that speed.

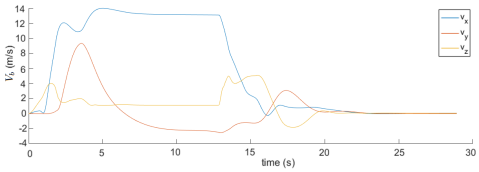

Figure 22: Hybrid Quadrotor speed

As the vehicle reaches aerodynamic attitude, will start to turn in towards the desired point. The controller allows for a significant side-slip, due to the maximum banking allowed for the vehicle being rather small, performing the curve with a radius of around $30m$.

During the final part of the flight, it does overshot the target position, due to its high linear momentum, but it is capable of compensating it and move to the desired position.

5.2 Results Hybrid Plane: In the case of the Hybrid Plane, the vehicle starts at position $[0\ 0\ 0]$, with z_b oriented with x_0 (fig. 23). The target point is $[10\ \ -400\ 0]$, with no fixed orientation.

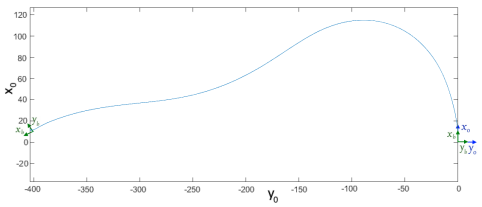

Figure 23: Hybrid Plane horizontal flight path

The Hybrid plane performs the turn with a radius of 120m. The controller is mainly using the control surfaces to perform the turn, which limits the vehicle turning rate. During the approach to the target position, it slightly overshoots it, but recovers to the desired position and stops.

The vehicle also takes more time to reach the maximum speed than the Hybrid Quadrotor (fig. 24), travelling further before starting to turn.

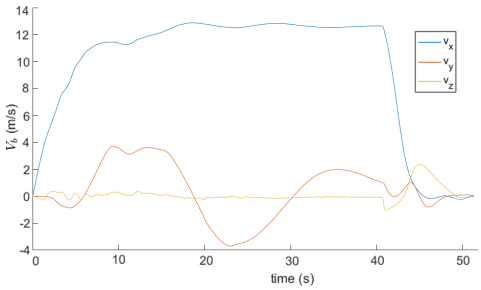

Figure 24: Hybrid Plane speed

6 Conclusions

The first main objective of this thesis was the creation of a model capable of representing in detail the dynamics of these types of vehicles. Special detail was necessary to handle the vehicle aerodynamics, as the vehicles are subjected to a wider range of conditions. For the wings, the model proposed provides a close approximation to the real word by using experimental data for the coefficients, and the discretization of the wing allows the effects of the vehicle rotation to be incorporated.

The propeller aerodynamics also have a major impact in the vehicle response. From the analysis to the models proposed, the difference in the approximations taken have a significant impact in the results for the propeller. The propellers are subject to significant lateral airflow, affecting the thrust and torque generated, and generating transverse moments. They will also reach conditions of very high advance ratio, as the propellers of the hybrid plane are gradually turned off during the transition .

The final model for the propellers is one of the major contribution from this thesis to the area of hybrid vehicles, and propellers in general. The inclusion of the effects of external airflow, a quadratic approximation for the lift coefficient, and including the transverse moments generated due to the unbalance in the thrust generated, provides a closer approximation to real world results.

The model implemented in Simulink^{TM} is not specific just for these two vehicles, it can be used to simulate a wide variety of vehicles, within certain restrictions.

From the vehicles trim analysis the range increase in Forward flight is clear, and which are the more efficient propellers for each vehicle. It is not possible however to conclude which is the more efficient approach, as the results are too close and some of the parameters of the vehicles, such as the weight, are mere estimations.

Another of the main objectives was to implement a control strategy capable of transitioning the vehicles trough the flight modes and able to handle disturbances. The implemented strategy proves enough to stabilise and control the vehicles in the presence of disturbances and with all the non linearities and irregularities present in the implemented model.

From here, one of the next steps would be implementing the model for the sensors and filters, and implement a controller using only the variables available from the sensors. Another step would be construction and testing of a real world prototype, to provide further validation to the model proposed, including an in depth analysis of the propellers performance.

References

[1] William J. Fredericks, Mark D. Moore, and Ronald C. Busan. Benefits of hybrid-electric propulsion to achieve 4x increase in cruise efficiency for a vtol aircraft. International Powered Lift Conference, 2013.

[2] Yann Ameho. *Du pilotage d'une famille de drones à celui d'un drone hybride via la commande adaptative*. PhD thesis, Institut Supérieur de l'Aéronautique et de l'Espace, 2013.

[3] Xinhua Wang and Lilong Cai. Mathematical modeling and control of a tilt-rotor aircraft. *Aerospace Science and Technology*, 47:473–492, October 2015.

[4] F. P. Beer and E. R. Johnston. *Vector Mechanics for Engineers*. McGraw-Hill, 7^{th} edition, 2006.

[5] J. Gordon Leishman. *Principles of Helicopter Aerodynamics*. Cambridge University Press, 2^{nd} edition, 2006.

[6] Tommaso Bresciani. *Modelling, Identification and Control of a Quadrotor Helicopter*. PhD thesis, Lund University, 2008.

[7] Andrew H. Lind, Jonathan N. Lefebvre, and Anya R. Jones. Time-averaged aerodynamics of sharp and blunt trailing edge static airfoils in reverse flow. *AIAA JOURNAL*, 52(12):2751–2764, December 2014.

[8] Karolin Schreiter. Development and validation of a generic flight simulation based on aircraft geometry. American Institute of Aeronautics and Astronautics, 2011.